RSC Advances

ROYAL SOCIETY OF CHEMISTRY

www.rsc.org/advances

A table of contents entry

Text: $SrTiO_3$ based CdS quantum dot sensitized solar cells exhibit higher *FF* and V_{OC} than the TiO_2.

Colour graphic:

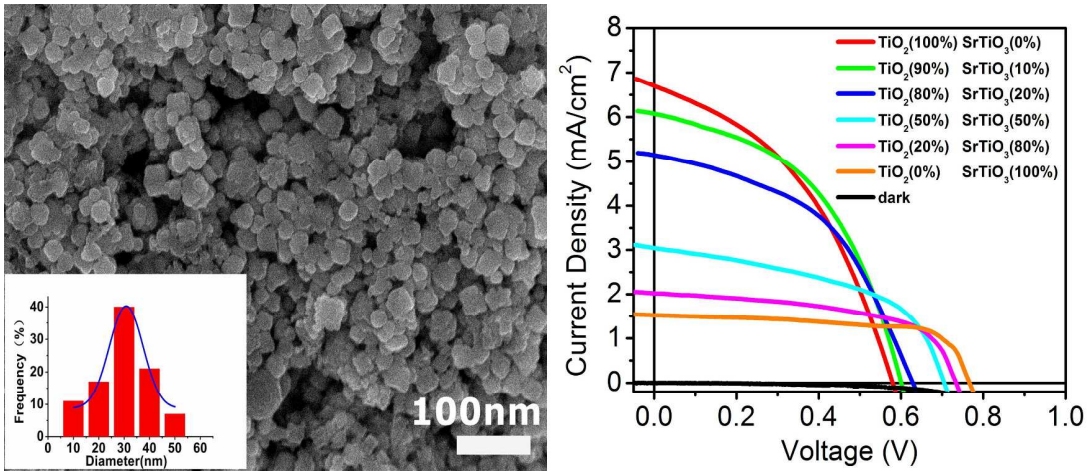

Journal Name

RSCPublishing

ARTICLE

Strontium Titanate Nanoparticles as Photoanode for CdS Quantum Dot Sensitized Solar Cells

Cite this: DOI: 10.1039/x0xx00000x

Cong Chen[a], Qilin Dai[a,*], Chuang Miao[a], Lin Xu[a], and Hongwei Song[a,*]

Received 00th January 2012,
Accepted 00th January 2012

DOI: 10.1039/x0xx00000x

www.rsc.org/

$SrTiO_3$ has the potential to be used as photoanode for quantum dot sensitized solar cells (QDSSCs) since it has very similar band structures to TiO_2 that exhibits the best performance in QDSSCs. In this work, $SrTiO_3$ nanoparticles (NPs) with a cubic crystal structure were prepared by hydrothermal method. 120, 70 and 30 nm $SrTiO_3$ NPs were obtained by using different starting materials. CdS quantum dots (QDs) were coated on three different sized $SrTiO_3$ NPs by successive ion layer adsorption and reaction (SILAR) method. QDSSCs based on three different sized $SrTiO_3$ NPs were fabricated and investigated. Due to the higher surface area compared to larger NPs, the device based on 30 nm $SrTiO_3$ NPs show the best open-circuit voltage (*Voc*) of 0.76 V and fill factor (*FF*) of 67% which are the relatively high *Voc* and FF reported in CdS-QDSSCs. Comparison studies of light-harvesting efficiency, electron transfer processes and band diagrams are performed to analyze the device performance in the $SrTiO_3$-QDSSCs and TiO_2-QDSSCs. The 30 nm $SrTiO_3$ NPs can be combined with TiO_2 NPs (P25) to improve the performance of CdS-QDSSCs with an increasing percentage of 12.5%, which represents an alternative way to realize high efficiencies in QDSSCs.

Introduction

QDSSCs have attracted substantial research interests due to the unique optical and electrical properties of the quantum dots (QDs) as light absorbers for solar cell applications.[1-3] It's believed that QDSSCSs have the possibility of circumventing the Shockley-Queisser efficiency limit for solar cells based on p−n junctions.[4] In addition, QDs with different sizes also have the capability to match the solar spectrum and improve light absorption. Most recently QDSSCs with efficiency as high as 8.55% have been achieved.[5] Various components in QDSSCs can be optimized in the actual process of assembly, photoanode material as an important area of research gets extensive attention recently. Usually, The

photoanodes in QDSSCs are usually binary metal oxides, such as TiO_2 or ZnO NPs. In comparison with binary metal oxides, ternary oxides, for example, $SrTiO_3$, exhibit better corrosion resistance and offer more freedom in tuning of optical and electrical properties.[6, 7]

$SrTiO_3$ can be roughly considered as a highly doped anatase TiO_2 because they have similar structures.[8] $SrTiO_3$ with perovskite structure contains titanium atoms in 6-fold octahedral coordination, which is similar to the titanium arrangement in anatase TiO_2. The two materials have exactly the same band gap, but $SrTiO_3$ has a slightly higher flat band potential, which could lead to higher *Voc* for the QDSSCs based on $SrTiO_3$ compared to that based on TiO_2. With higher flat band potential, $SrTiO_3$ has the capability of photoassisted electrolysis of water in comparison with anatase TiO_2.[9] Higher electron mobility in $SrTiO_3$（6.35 cm^2/vs）[10]compared to that in TiO_2 （0.1 cm^2/vs）[11] would be favorable for reducing recombination loss and for electron transport. Thus $SrTiO_3$ is a very promising photoanode in QDSSCs. Burnside *et al.* evaluated the feasibility of $SrTiO_3$ NPs with size range of 10-60 nm in the application of dye sensitized solar cells.[8] However, thus far, there have been few reports on $SrTiO_3$ applications in QDSSCs.

In this work, ternary oxide $SrTiO_3$ NPs with different sizes were prepared by hydrothermal method. Structural characterizations were carried out to examine the size, and crystalline structure of the as synthesized $SrTiO_3$ NPs. The QDSSCs based on $SrTiO_3$ NPs and CdS quantum dots were fabricated and characterized. 30 nm $SrTiO_3$ NPs show promising device performance. In addition, $SrTiO_3$ NPs can also be used to improve the device performance of TiO_2-QDSSCs due to the high *Voc* and *FF* of the devices based on $SrTiO_3$. Thus the first role of $SrTiO_3$ in this work is that it can be used as photoanode in QDSSCs. The second role is that $SrTiO_3$ NPs can also be used to improve the device performance of TiO_2-QDSSCs because TiO_2-QDSSCs have the best device performance till now.

Experiments section

Synthesis of $SrTiO_3$ NPs

$SrTiO_3$ NPs with different sizes were synthesized by hydrothermal method following previously published procedures.[8, 12, 13] 120, 70 and 30 nm $SrTiO_3$ NPs were prepared using titanium dioxide (P25), tetrabutyl titanate, and titaniumbis (ammonium lactate) dihydroxide (TALH) as starting materials, respectively. The experimental details can be found in supporting information.

Solar cell preparation

In the preparation of the $SrTiO_3$ photoanodes, $SrTiO_3$ powders were ground in a mortar with a few drops of glacial acetic acid and sufficient amount of ethanol for 20 minutes. Then the ground $SrTiO_3$ powders were dispersed in 30 ml of ethanol and ultrasonically agitated for 30 minutes to make $SrTiO_3$ paste. The detailed steps of $SrTiO_3$ composite paste preparation procedure are described in supporting information (Fig. S1).After that, the $SrTiO_3$ paste was spread onto 0.5 × 0.5 cm^2 (active area 0.25 cm^2) conducting FTO glass substrate by blade method and heated to 150 ℃ then sintered at 500 ℃ in a furnace for 30 minutes. The thickness of the photoanode is about 4 μm, which can be found from the cross section scanning electron microscope (SEM) image (Fig.S2). CdS QDs were coated on $SrTiO_3$ photoanode, using the successive ionic layer adsorption and reaction (SILAR) method following the procedure reported previously.[14] Specifically, the $SrTiO_3$/FTO substrate was successively immersed into 0.05 M $Cd(NO_3)_2$ in methanol and then into 0.05 M Na_2S in methanol for 2 minutes each. Following each immersion, the substrate was rinsed in pure methanol for 2 minutes to remove excessive precursors and then was dried before the next dipping to finish one CdS coating cycle. The above process was repeated to coat the QDs with different SILAR cycles to get four to eight layers of CdS. QDSSCs were fabricated by clamping a Cu_2S sputtered FTO glass plate onto a CdS QDs coated photoanode and filling the capillary space with the electrolytes (1 M Na_2S + 1 M S，18 MΩ deionized water). For comparison, the devices based on TiO_2 and $SrTiO_3$ /TiO_2 photoanodes were prepared by the same method.

Measurements

X-ray diffraction (XRD) patterns of all the $SrTiO_3$ powders were recorded on a RigakuD/max 2550 X-ray diffractometer, using a monochromatized Cu target radiation source at a scanning rate of 4^o/minute. SEM images were obtained from a SIRION field-emission scanning electron microscope. The transmission electron microscope (TEM) data were measured on a JEM-2010 with and the working voltage of 200 kV. *J-V* characteristics of the cells were recorded using a Keithley 2400 source meter and a 1.5 AM, 100 mW /cm^2 solar simulator lamp. Incident photon to current conversion efficiency (IPCE) was recorded using a computerized setup consisting of Solar Cell Quantum Efficiency ——SolarCellScan100. Absorption spectra were recorded with the Shimadzu UV-1600 Spectrophotometer. Electrochemical impedance spectroscopy (EIS) measurements were performed using an impedance measurement unit (ZAHNER-elektrik IM6) in the frequency range of 0.1–10^5 Hz, and the applied bias voltage and AC amplitude were set as the open-circuit voltage of the cells and 10 mV between the counter electrode and the working electrode, respectively. The nitrogen adsorption/desorption isotherms were measured at-196 ˚C with a Gemini VII surface area and porosity system. The specific surface area was estimated by the Brunauer–Emmett–Teller (BET) method.

Results and Discussion

Structure and morphology

The crystal structure of the $SrTiO_3$ NPs was characterized by XRD patterns, as shown in Fig. 1. All the XRD patterns of the $SrTiO_3$ NPs can be indexed to the cubic structure (JCPDS card 35-734) with well-defined (100), (110), (111), (200), (210), (211), (220) and (310) diffraction peaks. No other crystalline by-products can be observed in these XRD patterns.

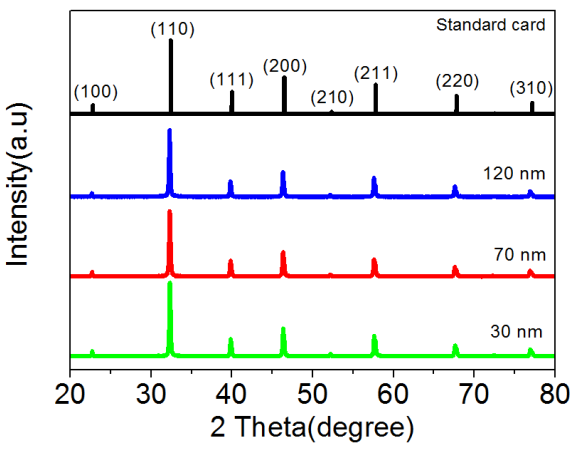

Fig. 1. XRD patterns of $SrTiO_3$ NPs with different sizes.

The XRD data of $SrTiO_3$ nanoparticles with different sizes look identical, which is consistent with the literature about 20-60 nm $SrTiO_3$ nanoparticles.[8, 12] Only sub-10 nm $SrTiO_3$ nanoparticles showed the broad XRD peaks.[13] Thus we believe that the XRD peaks may exhibit the features of broad peaks when the size of $SrTiO_3$ nanoparticles is below 10 nm.

Fig. 2 shows SEM and TEM images of the as synthesized $SrTiO_3$ NPs prepared with different starting materials and the inset shows the size distribution of the corresponding $SrTiO_3$ NPs. The sizes of the NPs distribute in a wide range for all the samples. From Fig. 2a and 2b it can be seen that as P25 and $Sr(OH)_2$ were chosen as starting materials, the products yield cube shaped NPs. The $SrTiO_3$ NPs have a diameter of 120 ± 32 nm (see inset of Fig. 2a). Fig. 2c shows the SEM image of the $SrTiO_3$ NPs prepared with tetrabutyl Titanate, $Sr(NO_3)_2$ and PVA. It can be seen that the shape of the NPs is irregular, and the size of the NPs is 70±8 nm. Fig. 2d shows the corresponding TEM image of Fig. 2c. From the boundary of the 70 nm NPs, it can be observed that they actually consist of a large number of smaller NPs with average size of 10 nm. The size and irregular shape of the as prepared NPs can be correlated to the additives-PVA. As a water-soluble polymer, PVA has been widely used to control the morphology and size in nanomaterial growth.[15, 16] Fig. 2e and 2f present, respectively, the SEM and TEM images of the $SrTiO_3$ NPs when TALH and $Sr(OH)_2{\cdot}8H_2O$ are used in the hydrothermal reaction. It is obvious that all the as-prepared NPs are composed of well-defined and relatively regular-shaped particles. The size of $SrTiO_3$ NPs is 30 ± 8.5 nm, which is comparable to that of TiO_2 (P25).

Device performance based on CdS QDs (four to eight cycles)

Current density *vs* voltage ($J-V$) characteristics of the devices sensitized by CdS QDs (four to eight cycles) based on different $SrTiO_3$ NPs (120, 70 and 30 nm) were obtained under AM 1.5G illumination with a light intensity of 100 mW /cm^2 and in the dark , as shown in Fig. 3a, 3b and 3c, respectively . For the QDSSCs based on 120 nm $SrTiO_3$ NPs, as shown in Fig. 3a, short-circuit photocurrent (J_{SC})

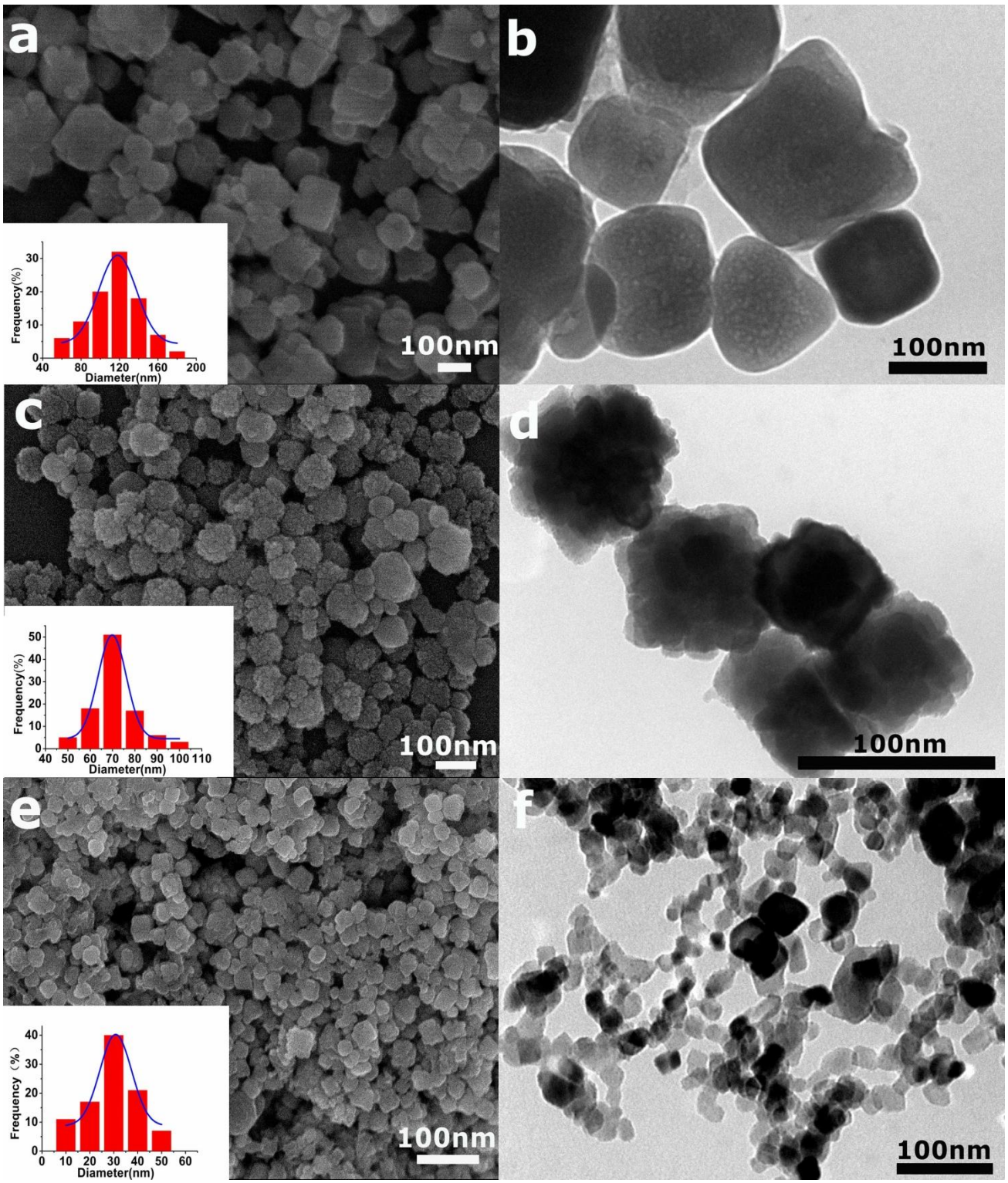

Fig. 2. SEM and TEM images of $SrTiO_3$ NPs with different sizes. (a) and (b) 120 nm $SrTiO_3$ NPs, P25 and $Sr(OH)_2$ were chosen as starting materials； (c) and (d) 70 nm $SrTiO_3$ NPs, synthesized by tetrabutyl titanate and $Sr(NO_3)_2$ and PVA； (e) and (f) 30 nm $SrTiO_3$ NPs，prepared by TALH and $Sr(OH)_2.8H_2O$.

increases from 0.28 to 0.56 mA/cm^2 and *Voc* increases from 0.54 to 0.72 V as the number of coating cycles increases from four to seven. However, J_{SC} and *Voc* decreases as the number of coating cycles increases to eight. Same trend is observed for the QDSSCs based on 70 and 30 nm $SrTiO_3$ NPs (Fig. 3b and c). J_{SC} increases from 0.52 to 0.94 mA/cm^2 and *Voc* increases from 0.42 to 0.74V as the number of coating cycles increases from four to seven for the QDSSC based on 70 nm $SrTiO_3$ NPs. J_{SC} increases from 0.76 to 1.53 mA/cm^2 and *Voc* increases from 0.50 to 0.76 V as the number of coating cycles increases from four to seven for the QDSSC based on 30 nm $SrTiO_3$ NPs. All devices exhibit the optimum results in the seventh cycle and appear decreased permanence in the eighth cycles. This phenomenon could be explained by the varied IPCE of the QDSSCs and the varied bandgap with CdS particle sizes, which will be discussed in the following text.

Fig. 4a shows the IPCE spectra of QDSSCs based on CdS QDs with different coating cycles on 70 nm $SrTiO_3$ NPs, which could be representative for that based on 120 and 30 nm $SrTiO_3$ NPs.

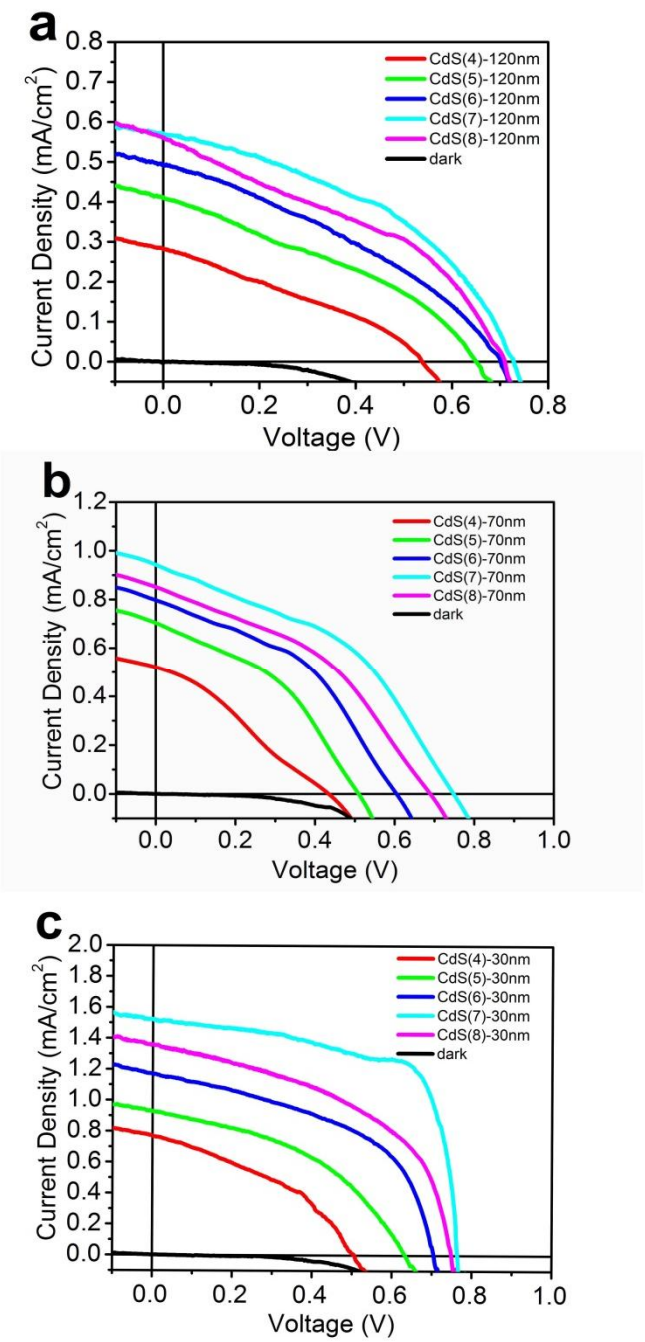

Fig. 3. (a) *J–V* characteristics of QDSSCs based on CdS QDs prepared with different coating cycles and 120 nm $SrTiO_3$ NPs. (b) *J–V* characteristics of QDSSCs based on CdS QDs prepared with different coating cycles and 70 nm $SrTiO_3$ NPs. (c) *J–V* characteristics of QDSSCs based on CdS QDs prepared with different coating cycles and 30 nm $SrTiO_3$ NPs.

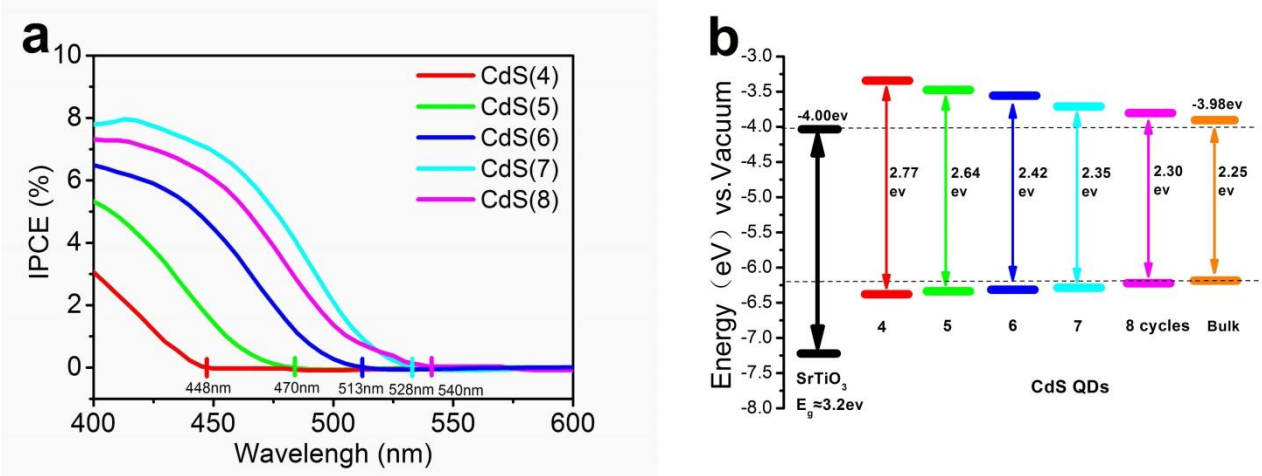

Fig. 4. (a) IPCE spectra of QDSSCs based on 70 nm $SrTiO_3$ NPs and CdS QDs coated using different SILAR cycles. (b) Bandgaps of CdS QDs prepared with different coating cycles and their band alignment with $SrTiO_3$.

Monotonic increase can be observed as the incident light wavelength is scanned from 600 to 400 nm without exhibiting distinctive excitonic features. The maximum intensity of IPCE increases when the number of the coating cycles increases from four to seven, however, the maximum intensity of IPCE decreases as the number of coating cycles increase to eight, which is well in accordance with the *J*–*V* characteristics. The absence of the CdS excitonic features in the IPCE spectra could be explained by the broad size distribution of the SILAR-based QDs.[14] The IPCE spectra also show onset wavelengths shift from 448 nm (four-cycle cell) to 540 nm (eight-cycle cell), which can be attributed to the increased QD size and decreased QD bandgap. According to the literature, the conduction band edges TiO_2 is ~4.2 eV below the vacuum level, the conduction band edge of bulk CdS is about 3.98 eV below the vacuum level.[17, 18] According to previously report，$SrTiO_3$ has a same bandgap of 3.2 eV as TiO_2 but lower the conduction band edge about 0.2 eV than that of TiO_2.[8] so the conduction band edge of $SrTiO_3$ is -4.0 eV vs. vacuum. Combing the literature results and IPCE test data, the band diagrams of $SrTiO_3$ nanoparticle, CdS QDs are shown in Fig. 4b. Size-dependent band gaps of CdS QDs are estimated by the onset wavelengths of the IPCE spectra (which are due to light absorption of CdS QDs[19]) It's

believed that the decrease of CdS bandgap is mainly caused by a downward shift of the conduction band edge due to large effective mass of the hole compared to that of the electron.[20, 21] From Fig. 4b, it can be observed that when the number of coating cycles increases from four to eight, the conduction band edge difference between CdS QD and $SrTiO_3$ gradually becomes smaller. The driving force for electron transfer at the QD/$SrTiO_3$ interface is dependent on the band edge difference. A reduced conduction band difference leads to decreased driving force and charge injection efficiency.[21]

Actually, as the number of coating cycles increases, on one hand, the light harvesting efficiency of the cell and the quantity of photo-generated electrons gradually increase, leading J_{SC} to increase; on the other hand, the driving force and charge injection efficiency gradually decrease, leading J_{SC} to decrease gradually. These two competing mechanisms induce the appearance of an optimum coating cycle (seven cycles) for the *J-V* response. Note that as the number of coating cycles increases to seven, the light harvesting efficiency of the cell does not increase with the increase of cycle number further, because the size confinement hardly takes efforts any more. In this case, the decreased driving force contributes dominantly to the solar cell performance

Device performance based on $SrTiO_3$ NPs with different sizes

Because the QDSSCs based on CdS QDs prepared with seven cycles demonstrates the optimum device permanence, in the following experiments the CdS QDs are all fixed at seven cycles. Fig. 5a shows the influence of $SrTiO_3$ particle size on the *J-V* characteristics of seven-cycle cells. It can be seen that when the size decreases from 120 to 30 nm, the short circuit photocurrent density J_{SC} almost increases three times, from 0.56 to 1.53 mA/cm^2. Concomitantly, the *Voc* increases from 0.72 to 0.76 V, and the *FF* increases from 0.48 to 0.67. The power conversion efficiency increases from 0.19% to 0.78%. The detailed device performance parameters are listed in Table 1. From Fig. 5a, the device with 30 nm $SrTiO_3$ NPs as photoanode shows the best device

Table 1. Parameters obtained from *J-V* measurements of the QDSSCs prepared with seven coating cycles

Architecture	Voc (V)	Jsc（mA/cm^2）	FF	η（%）
$SrTiO_3$ (30nm)	0.76	1.53	0.67	0.78%
$SrTiO_3$ (70nm)	0.74	0.94	0.51	0.35%
$SrTiO_3$ (120nm)	0.72	0.56	0.48	0.19%

performance of 0.78% with the highest *Voc* and *FF* reported in typical CdS-QDSSCs.[22, 23]

In order to reveal the origin of device performance changing with $SrTiO_3$ particle size, the absorption spectra and IPCE measurements based on the three kinds of best performance devices were designed.

The absorption spectra of CdS QDs, which are obtained by subtracting the blank (no QDs) device absorption from a working device absorption, are presented in Fig. 5b. It can be seen that the absorption intensities of CdS QDs increase when the size of $SrTiO_3$ NPs decreases, indicating that smaller $SrTiO_3$ NPs have higher QD coverage. Similar phenomenon was also observed for the QDSSCs based on TiO_2.[24] The inset of Fig. 5b shows the photographs of different sized $SrTiO_3$ NPs coated with seven-cycle CdS QDs. The coating of CdS QDs over $SrTiO_3$ is accompanied by color changes visible to the naked eye. The color becomes darker as smaller $SrTiO_3$ NPs are utilized for CdS QD coating, which confirms higher QD coverage on smaller $SrTiO_3$ NPs. Higher QD coverage leads to better device performance due to improved light harvesting efficiency of the cell. Fig. 5c shows the IPCE spectra of seven-cycle cells based on 120, 70 and 30 nm $SrTiO_3$ NPs. The maximum IPCE values increase from 5.7% to 15.6% as the size of NPs decreases following the same trend of *J-V* of QDSSCs (Fig. 5a). The IPCE spectra of CdS QDs are consistent with the corresponding absorption spectra, as shown in Fig. 5b. The onset wavelengths are very similar for devices based on the $SrTiO_3$ NPs of different sizes, which can be

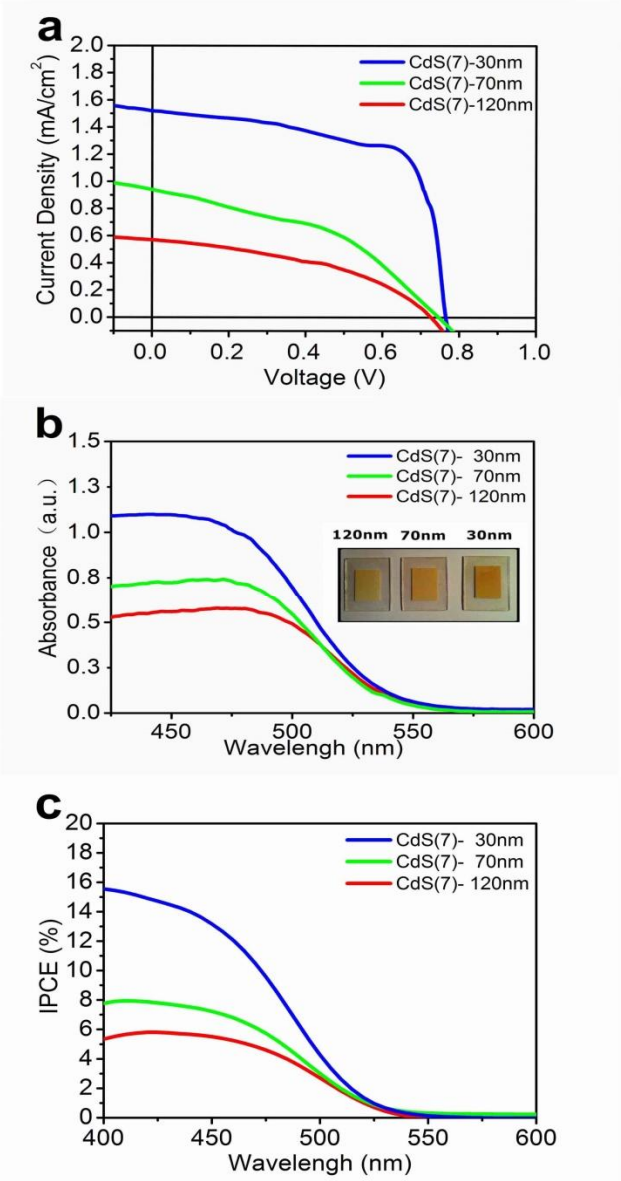

Fig. 5. (a) *J–V* characteristics of QDSSCs based on CdS QDs prepared with seven coating cycles and different sized $SrTiO_3$ NPs. (b) UV-vis absorption spectra of CdS QDs prepared with seven coating cycles on $SrTiO_3$ NPs with different sizes. The inset shows the photographs of CdS QDs prepared with seven coating cycles on 120, 70 and 30 nm $SrTiO_3$ NPs. (c) IPCE spectra of QDSSCs based on $SrTiO_3$ NPs with different sizes and CdS QDs coated using seven SILAR cycles.

observed in both IPCE and absorption spectra (Fig. 5b and c), indicating that the sizes of the QDs are the same for seven-cycle QDs. Although the average size of $SrTiO_3$ NPs changes, however, the size of QDs is only related to the number of SILAR coating cycles. This explains why different sized $SrTiO_3$-based QDSSC devices have the same ideal performance appeared in the seventh cycles.

Different intensities in IPCE and absorption spectra can be attributed to different QD adsorptions on $SrTiO_3$ NPs, and it is the dominant factor to influence the overall performance of the devices.

$TiO_2/SrTiO_3$ composite-based QDSSC device performance

It was reported that incorporating different materials and using their respective advantages had a great influence on the device performance.[25-27] In order to take advantage of the high *Voc* and *FF* characteristics of the device based on 30 nm $SrTiO_3$ NPs and the high current characteristics of TiO_2 based QDSSCs. QDSSCs based on $TiO_2/SrTiO_3$

Table 2. Parameters obtained from J-V measurements of the QDSSCs based on seven-cycle CdS QDs and TiO2/SrTiO3 composites. The average and standard deviation (s.d) values are obtained from a batch of 6 identically processed TiO2/SrTiO3 composite-based QDSSCs.

Architecture	**Voc (V)**	**Jsc（mA/cm²）**	**FF**	**η（%）**
TiO_2 (100%) $SrTiO_3$ (0%)	0.58 ± 0.03	6.6 ± 0.30	0.41 ± 0.01	1.6%± 0.15
TiO_2 (90%) $SrTiO_3$ (10%)	0.60 ± 0.02	6.0 ± 0.24	0.48 ± 0.02	1.8%± 0.18
TiO_2 (80%) $SrTiO_3$ (20%)	0.62 ± 0.02	5.0 ± 0.13	0.48 ± 0.01	1.5%± 0.16
TiO_2 (50%) $SrTiO_3$ (50%)	0.70 ± 0.03	3.0 ± 0.15	0.49 ± 0.05	1.0%± 0.20
TiO_2 (20%) $SrTiO_3$ (80%)	0.73 ± 0.05	2.0 ± 0.22	0.56 ± 0.02	0.82%± 0.15
TiO_2 (0%) $SrTiO_3$ (100%)	0.76 ± 0.06	1.53± 0.11	0.67 ± 0.03	0.78% ± 0.10

composite system at different quality ratios of TiO_2 to $SrTiO_3$ were fabricated and compared. Fig. 6a shows *J–V* curves of QDSSCs based on TiO_2/$SrTiO_3$ composite under AM 1.5G illumination with a light intensity of 100 mW /cm^2. The corresponding solar cell parameters are summarized in Table 2. Compared with pure TiO_2, the QDSSC exhibits higher *Voc* and *FF* but slightly small J_{SC} when the ratio of TiO_2 to $SrTiO_3$ is 9:1 leading to the energy conversion efficiency is enhanced from 1.6% to 1.8% with an improvement of 12.5%. As the ratio of TiO_2 to $SrTiO_3$ decreases further, *Voc* and *FF* increase but J_{SC} decreases, resulting in decreased conversion efficiency.

Mao *et al.* reported the enhanced photovoltaic response of TiO_2/$SrTiO_3$ composite compared to pure $SrTiO_3$ and TiO_2.[28] Improved separation efficiency of photogenerated carriers due to the matched energy levels of TiO_2 and $SrTiO_3$ were considered as one possible reason for the enhanced photovoltaic response. Reduced recombination rate of the composite was also proposed to explain the improved photovoltaic response, which was manifested by photoluminescence spectra.[28] In our case, the electrons will be injected into both $SrTiO_3$ and TiO_2 as $SrTiO_3$ was incorporated into TiO_2. The flat band potential of $SrTiO_3$ is higher than that of TiO_2, which leads to the higher *Voc* of the

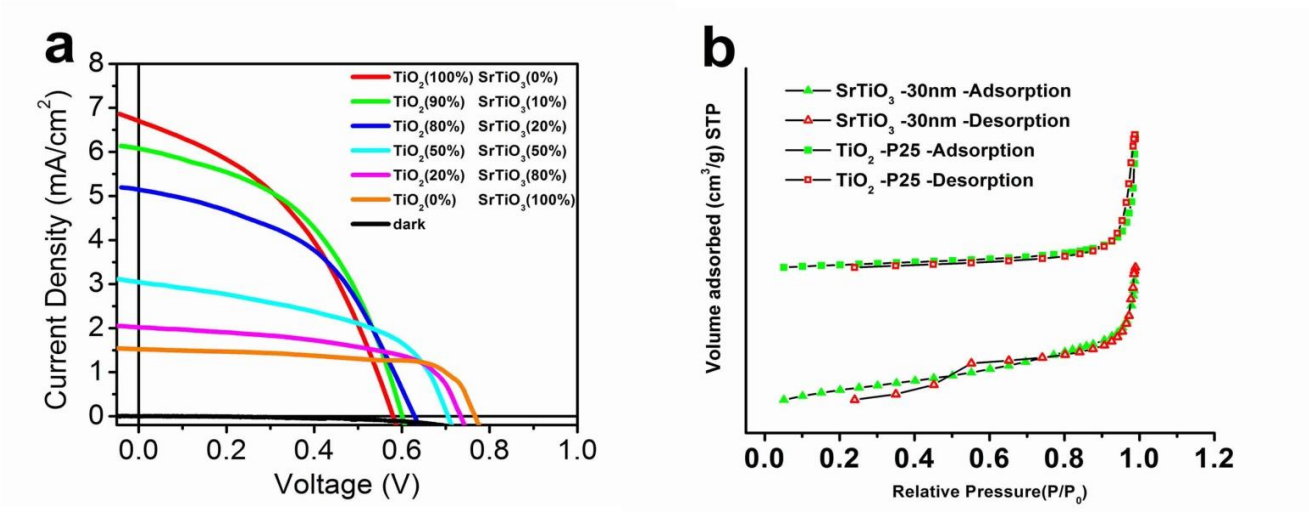

Fig. 6. (a) *J–V* characteristics of QDSSCs based on CdS QDs prepared with seven coating cycles and TiO_2/$SrTiO_3$ composites with different ratios. (b) Nitrogen adsorption-desorption isotherm of 30 nm $SrTiO_3$ NPs and TiO_2.

device based on TiO_2/$SrTiO_3$ composite. In addition, according to Mao's results, the recombination rate in TiO_2/$SrTiO_3$ composite can be reduced compared to pure TiO_2, which results in larger *FF*. The power conversion efficiency is determined by J_{SC}, *FF* and *Voc*. The J_{SC} of the QDSSCs based on TiO_2/$SrTiO_3$ composite is smaller than that for pure TiO_2. However, *FF* and *Voc* can be increased due to the band alignment and reduced recombination rate. Thus it is very possible that the power conversion efficiency of QDSSCs based on TiO_2 can be improved as appropriate amount of $SrTiO_3$ is used in the composite.

Meng *et al.* investigated CdS/CdSe-sensitized solar cells controlled by the structural properties of compact porous TiO_2 photoelectrodes, and achieved a high FF (61%-65%). They explained that by extending the light path length and decreasing the electron recombination caused by the scattering layer.[29] It was also reported that high FF (56%) could be obtained by using ordered multimodal porous carbon as counter electrode in QDSSCs, and that was attributed to the low charge transfer resistance and Nernst diffusion impedance of the counter electrodes.[30] Emin *et al.* obtained a high FF of 60% and attributed that to the low series resistances of the FTO/TiO_2 films[3]. In our study

(see Table 3), the series resistance of FTO/$SrTiO_3$ (35.1 Ω) is very similar to that of FTO/TiO_2 (35.6 Ω). However, the charge transfer resistance of the device based on $SrTiO_3$ is 924 Ω which is smaller than that of TiO_2 (1149 Ω). Thus we think the low charge transfer resistance leads to high FF for the device based on $SrTiO_3$ in comparison with the TiO_2-based device. Kang *et al.* reported a high *Voc* of 0.77 V by reducing the recombination process via a novel photoanode architecture of "pine tree" ZnO nanorods on Si nanowires hierarchical branched structure.[31] Self-assembled monolayers were used as recombination barriers to realize high efficiency of the devices and the high V_{oc}.[32] In our recent work, we used rare earth ions to modulate the band gap of the photoanode in dye sensitized solar cells to increase V_{oc}. [33] We think the main reason for the high V_{oc} of the devices based on $SrTiO_3$ is higher flat band potential.

J_{SC} is mainly determined by light-harvesting efficiency and charge injection efficiency. Light-harvesting efficiency is correlated with the adsorption capacity of photoanode, and adsorption capacity is determined by higher specific surface area. Nitrogen adsorption measurement is designed to measure the specific surface area of samples, the nitrogen adsorption/desorption isotherms based on $SrTiO_3$ (30nm) and TiO_2 （P25） samples are plotted in Fig. 6b, The BET surface areas for the $SrTiO_3$ and TiO_2 are reported to be 40 and 51 m^3/g respectively by the nitrogen adsorption/desorption measurements. Thus the adsorption ability of 30 nm $SrTiO_3$ is lower than that of P25 due to the difference in surface areas. The surface areas of 120 nm and 70 nm $SrTiO_3$ NPs are 7.1 and 15.7 m^3/g respectively. This further explains the lower *J-V* and *IPCE* of the devices based 120 nm and 70 nm $SrTiO_3$ NPs compared to that based on 30 nm $SrTiO_3$ NPs shown in Fig. 5a and Fig. 5c.

To study the adsorption ability of $SrTiO_3$ compared to TiO_2. Oxide photoanodes coated with CdS QDs by SLIAR process were put into 50 mL dilute nitric acid for two hours to dissolve CdS QDs and to produce Cd^{2+}. A VA Computrace (TEA 4000) was used to detect the concentration of Cd^{2+}, and the results are listed in Table S1. It can be

Table 3. Fitting results of the Nyquist Plot.

Photoanode	Rs (Ω)	R_1 (Ω)	CPE_1	R_2 (Ω)	CPE_2
$SrTiO_3$	35.1	924	1.073E-5	1528	2.318 E-4
TiO_2	35.6	1149	1.052E-5	3874	5.956 E-4

observed that concentration of Cd^{2+} increases when the ratio of TiO_2 to $SrTiO_3$ increases. The concentration of Cd^{2+} taken by $SrTiO_3$ is lower compared to that of TiO_2, which indicates that $SrTiO_3$ has lower adsorption ability. Thus the low J_{SC} of the QDSSC based on $SrTiO_3$ could be partially attributed to low adsorption ability of $SrTiO_3$ compared to TiO_2.

EIS study of $SrTiO_3$-QDSSCs and TiO_2-QDSSCs

Comparison study of the electron transfer processes in the $SrTiO_3$-QDSSCs and TiO_2-QDSSCs was carried out by EIS measurements. Typical Nyquist plots of $SrTiO_3$-QDSSCs and TiO_2-QDSSCs are shown in Fig. 7. The inset shows the equivalent circuit which is used to fit the Nyquist plot according to Ref [34]. A smaller semicircle in high frequency region (around 100 Hz) and a larger semicircle in low frequency region (around 1 Hz) can be clearly observed. Each semicircle indicating a charge transfer process exhibited by a resistance capacitance (R-C) parallel circuit. For a more precise fitting, the capacitance element is replaced by a constant phase element (CPE). R_s, R_1 and R_2 values are listed in Table 3, which are determined by fitting according to the equivalent circuit. R_s is the device ohmic series resistance, which is contributed by the sheet resistance of the substrates, resistivity of the electrolyte, and electrical contacts of the cell. R_1 and CPE_1 stand for the charge transfer resistance and double layer capacitance at the electrolyte/counter electrode interface.[34] R_2 and CPE_2 represents the recombination charge transfer resistance and chemical capacitance at the photoanode/QDs/electrolyte interface.[29] Rs value for the $SrTiO_3$-QDSSCs is 35.1Ω, which is similar

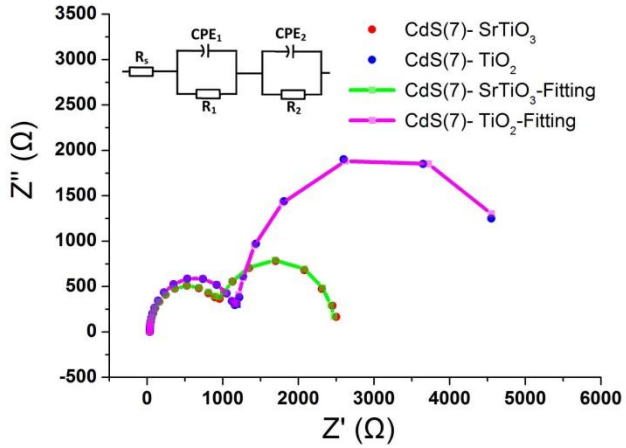

Fig. 7. Nyquist plots of QDSSCs. The inset is the equivalent circuit. The scattered points are experimental data and the solid lines are the fitting curves.

to that of TiO_2-QDSSCs (35.6Ω), this indicates that $SrTiO_3$-QDSSCs and TiO_2-QDSSCs have the same device configuration. R_1 value for the $SrTiO_3$-QDSSCs is 924Ω, which is a little smaller compared to that of TiO_2-QDSSCs (1149Ω). The R_2 values of the $SrTiO_3$-QDSSC and TiO_2-QDSSC are 1528 Ω and 3874 Ω respectively. The higher R_2 implies the less recombination of electrons between the electrolyte and the conduction band of photoanode that is expected.[29] This result reveals that the recombination of electrons in $SrTiO_3$-QDSSCs is higher than TiO_2-QDSSCs, leading to lower J_{SC} in $SrTiO_3$-QDSSCs.

The driving force analysis between $SrTiO_3/TiO_2$ and CdS QD

Fig. 8 shows the band diagrams and the estimated conduction band edges of $SrTiO_3$, TiO_2 and CdS QDs (seven cycles). According to previous discussion and described in Fig. 4b, the conduction band edge of the CdS QDs is estimated ~0.1 and ~0.3 eV higher than that of the $SrTiO_3$ and TiO_2 respectively, which will make the charge injection from QDs to $SrTiO_3$ or TiO_2 possible. The conduction band edge of $SrTiO_3$ is 0.2 eV higher than that of TiO_2, leading to higher position of Fermi level in $SrTiO_3$, which is related to larger *Voc* of the QDSSCs based on $SrTiO_3$ according to the *Voc* analysis in theory as follows.

According to experimental results and theoretical calculations, although the *Voc* is determined by many factors inside the cell, the open circuit voltage of QDSSCs can be estimated by:[35, 36]

$$Voc = E_g - \Delta_1 - \Delta_2 ,$$

where E_g is the bandgap of CdS QDs,Δ_1 represents the energy difference between the conduction band of the CdS QDs and the

conduction band of the semiconductor oxide（TiO_2 or $SrTiO_3$）; Δ_2 is the energy difference between oxidized redox potential of the electrolyte and the valence band of the CdS QDs. Compared with the conventional TiO_2, $SrTiO_3$ is caused the reduction ofΔ_1, this will lead to improvement of the *Voc* of device. Therefore, the QDSSCs based on $SrTiO_3$ have a higher open circuit voltage than that based on TiO_2. However, Δ_1 can determine the driving force for the charge injection from QDs to $SrTiO_3$. So it will also result in small driving force for the charge injection from QDs to $SrTiO_3$. In addition, charge recombination process happens synchronously when Δ_1 decreases. These two factors would partially contribute to the low device performance compared to TiO_2-QDSSCs. In a word, the low J_{SC} of $SrTiO_3$-QDSSCs can be attributed to smaller surface area of the $SrTiO_3$ NPs, smaller driving force due to the higher flat band potential and smaller recombination charge transfer resistance of the device. Thus both of higher *Voc* and lower J_{SC} are originated from the flat band potential of $SrTiO_3$ which leads to the lower device performance.

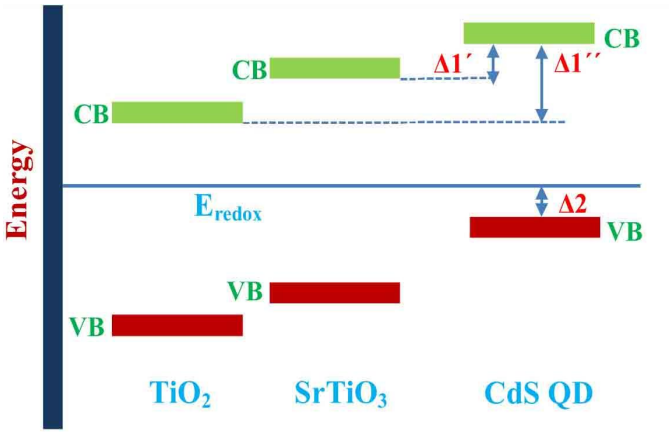

Fig. 8. Band alignment of $SrTiO_3$, TiO_2 and CdS QDs prepared with seven cycles. (Note that band positions are for reference only and not drawn to precise scale.)

Conclusions

In summary, in this work, $SrTiO_3$ NPs with different sizes were synthesized by hydrothermal method and utilized as the photoanode in QDSSCs. CdS QDs were deposited on the NPs using the SILAR approach. Device performance of the QDSSCs was studied, and the highest *Voc* of 0.76 V and *FF* of 67% were observed for the cells prepared with seven coating cycles on 30 nm $SrTiO_3$ NPs. IPCE measurements were carried out to inspect CdS bandgaps and alignment with $SrTiO_3$ NPs. Through nitrogen adsorption measurement, it proves that 30 nm $SrTiO_3$ NPs have a surface area of 40 m^3/g, which is smaller

than that of P25 (51 m^3/g). Improved device performance of TiO_2-QDSSCs was observed as 30 nm $SrTiO_3$ NPs was incorporated into TiO_2, which can be attributed to the high *Voc* of $SrTiO_3$-QDSSCs caused by their band structure and larger *FF* due to reduced recombination rate. That points to a new method to improve the solar cell efficiency. EIS measurements for $SrTiO_3$-QDSSC and TiO_2-QDSSC were also carried out to study electron transport and recombination processes in the QDSSCs. Smaller recombination charge transfer resistance was observed for $SrTiO_3$-QDSSC compared to TiO_2-QDSSC, which can result in lower device performance. The first scientific significance of QDSSC fabrication with the $SrTiO_3$ is $SrTiO_3$ nanoparticles can be used as photoanode for QDSSCs, and the devices based on $SrTiO_3$ show high *Voc* and *FF* compared to other QDSSCs. The second one is that $TiO_2/SrTiO_3$ composites were developed to improve the TiO_2-QDSSC device performance by using the high *Voc* and *FF* of $SrTiO_3$-QDSSCs.

Acknowledgements

This work was supported by the Major State Basic Research Development Program of China (973 Program) (No. 2014CB643506), the National Natural Science Foundation of China (Grant no. 11374127, 11304118, 61204015, 81201738, 81301289, 61177042, and 11174111), Program for Chang Jiang Scholars and Innovative Research Team in University (No. IRT13018). The China Postdoctoral Science Foundation Funded Project (2012M511337 and 2013T60327).

Notes and references

1. D.-M. Li, L.-Y. Cheng, Y.-D. Zhang, Q.-X. Zhang, X.-M. Huang, Y.-H. Luo and Q.-B. Meng, *Sol. Energy Mater. Sol. Cells*, 2014, 120, Part B, 454-461.
2. G. Seo, J. Seo, S. Ryu, W. Yin, T. K. Ahn and S. I. Seok, *J. Phys. Chem. Lett.*, 2014, 5, 2015-2020.
3. S. Emin, M. Yanagida, W. Peng and L. Han, *Sol. Energy Mater. Sol. Cells*, 2012, 101, 5-10.
4. O. E. Semonin, J. M. Luther, S. Choi, H.-Y. Chen, J. Gao, A. J. Nozik and M. C. Beard, *Science*, 2011, 334, 1530-1533.
5. P. R. B. Chia-Hao M. Chuang and M. G. B. Vladimir Bulović, *nature*, 2014.
6. B. Tan, E. Toman, Y. Li and Y. Wu, *J. Am. Chem. Soc.*, 2007, 129, 4162-4163.
7. Y. Zhang, H. Zhang, Y. Wang and W. Zhang, *J. Phys. Chem. C*, 2008, 112, 8553-8557.
8. S. Burnside, J.-E. Moser, K. Brooks, M. Grätzel and D. Cahen, *J. Phys. Chem. B*, 1999, 103, 9328-9332.
9. H. O. Finklea, *Semiconductor electrodes*, Elsevier Science Ltd, 1988.
10. R. M. W. M. K. H. Härdtl, *Appl. Phys. A*, 1995, 61, 6.
11. P. Tiwana, P. Docampo, M. B. Johnston, H. J. Snaith and L. M. Herz, *Acs. Nano*, 2011, 5, 5158-5166.
12. X. Wei, G. Xu, Z. Ren, C. Xu, G. Shen and G. Han, *J. Am. Ceram. SOC.*, 2008, 91, 3795-3799.
13. K. Fujinami, K. Katagiri, J. Kamiya, T. Hamanaka and K. Koumoto, *Nanoscale*, 2010, 2, 2080-2083.
14. H. Lee, M. Wang, P. Chen, D. R. Gamelin, S. M. Zakeeruddin, M. Graetzel and M. K. Nazeeruddin, *Nano. Lett.*, 2009, 9, 4221-4227.
15. H. Yu, X. Xu, X. Chen, T. Lu, P. Zhang and X. Jing, *J. Appl. Polym. Sci.*, 2007, 103, 125-133.
16. D. Guin, S. V. Manorama, J. N. L. Latha and S. Singh, *J. Phys. Chem. C*, 2007, 111, 13393-

13397.
17. H. Lee, H. C. Leventis, S.-J. Moon, P. Chen, S. Ito, S. A. Haque, T. Torres, F. Nueesch, T. Geiger, S. M. Zakeeruddin, M. Graetzel and M. K. Nazeeruddin, *Adv. Funct. Mater.*, 2009, 19, 2735-2742.
18. T. Lv, L. Pan, X. Liu, T. Lu, G. Zhu, Z. Sun and C. Q. Sun, *Catal. Sci. Technol.*, 2012, 2, 754-758.
19. Q. Dai, J. Chen, L. Lu, J. Tang and W. Wang, *Nano. Lett.*, 2012, 12, 4187-4193.
20. K. Tvrdy, P. A. Frantsuzov and P. V. Kamat, *Proc. Natl. Acad. Sci.*, 2011, 108, 29-34.
21. G. Rothenberger, D. K. Negus and R. M. Hochstrasser, *J. Chem. Phys.*, 1983, 79, 5360-5367.
22. T. Bora, H. H. Kyaw and J. Dutta, *Electrochim. Acta.*, 2012, 68, 141-145.
23. Q. Zhang, Y. Zhang, S. Huang, X. Huang, Y. Luo, Q. Meng and D. Li, *Electrochim. Commun.*, 2010, 12, 327-330.
24. A. Kongkanand, K. Tvrdy, K. Takechi, M. Kuno and P. V. Kamat, *J. Am. Chem. Soc.*, 2008, 130, 4007-4015.
25. B. C. O'Regan, S. Scully, A. C. Mayer, E. Palomares and J. Durrant, *J. Phys. Chem. B*, 2005, 109, 4616-4623.
26. A. Kay and M. Gratzel, *Chem. Mater.*, 2002, 14, 2930-2935.
27. K. Tennakone, G. K. R. Senadeera, V. P. S. Perera, I. R. M. Kottegoda and L. A. A. De Silva, *Chem. Mater.*, 1999, 11, 2474-2477.
28. Y. T. Zheng, Z. L. Zhang and Y. L. Mao, *J. Alloy. Compd.*, 2013, 554, 204-207.
29. Q. Zhang, X. Guo, X. Huang, S. Huang, D. Li, Y. Luo, Q. Shen, T. Toyoda and Q. Meng, *Phys. Chem. Chem. Phys.*, 2011, 13, 4659-4667.
30. S.-Q. Fan, B. Fang, J. H. Kim, B. Jeong, C. Kim, J.-S. Yu and J. Ko, *Langmuir*, 2010, 26, 13644-13649.
31. P. Sudhagar, T. Song, D. H. Lee, I. Mora-Seró, J. Bisquert, M. Laudenslager, W. M. Sigmund, W. I. Park, U. Paik and Y. S. Kang, *J. Phys. Chem. Lett.*, 2011, 2, 1984-1990.
32. P. Ardalan, T. P. Brennan, J. R. Bakke and S. F. Bent, in *Photovoltaic Specialists Conference (PVSC), 2010 35th IEEE*, 2010, pp. 000951-000954.
33. C. Miao, C. Chen, Q. Dai, L. Xu and H. Song, *Journal of Colloid and Interface Science*, 2015, 440, 162-167.
34. Z. Huang, G. Natu, Z. Ji, P. Hasin and Y. Wu, *J. Phys. Chem. C*, 2011, 115, 25109-25114.
35. H. J. Snaith, *Adv. Funct. Mater.*, 2010, 20, 13-19.
36. J. Zhang, H.-B. Li, S.-L. Sun, Y. Geng, Y. Wu and Z.-M. Su, *J. Mater. Chem.*, 2012, 22, 568-576.